

Finite strip modeling of the varying dynamics of thin-walled pocket structures during machining

Keivan Ahmadi¹

Received: 28 March 2016 / Accepted: 12 May 2016 / Published online: 26 May 2016
© Springer-Verlag London 2016

Abstract The structural model of the workpiece is required for modeling, analysis, and avoidance of forced and regenerative (chatter) vibrations in machining of thin-walled parts. Finite element models (FEM) provide a versatile means for modeling the workpiece dynamics, but such models need to be updated frequently as the mass and stiffness of the workpiece varies continuously during machining. The computational time and power that is needed for re-meshing the FEM and then re-computing the natural modes of the workpiece is prohibitive. In this paper, a new approach based on Finite strip modeling (FSM) is presented for modeling the structural dynamics of thin-walled structures during pocket milling operations. The substantially higher computational efficiency of the FSM approach in predicting the varying dynamics of thin-walled pocket structures is verified by comparing its performance against FEM and the multi span plate (MSP) approach presented in (J Manuf Sci Eng 133:021014, 2011). Additionally, the accuracy of the presented approach in analyzing the stability of vibrations and determining the extent of dynamic deflections is verified using experimental results.

Keywords Vibration · Chatter · Varying dynamics · Structural analysis

1 Introduction

Thin-walled structures are commonly found in aerostructures such as spars, ribs, and skin. The high flexibility of thin-walled structures makes them prone to dynamic deflections and vibration instability (chatter) in semi-finishing and finishing stages of machining. While various approaches [1–5] are available in the literature to model the structural dynamics of machine tools, modeling the structural dynamics of flexible thin-walled workpieces is an open problem. The main obstacle in modeling the vibrations of thin-walled machining is the variation of the mass and stiffness of the structure as the material is being removed. Finite element models (FEM) are usually used for structural modeling of flexible workpieces [6–9], but as the wall thickness decreases during machining, the FEM needs to be updated by re-modeling the structure, re-meshing the model, and re-computing the natural modes. As shown in [8], updating FEM at different stages of machining is computationally prohibitive and thus alternative approaches are required to efficiently model the varying dynamics of the workpiece.

FEM has been used in several studies to simulate the varying dynamics of the workpiece in different stages of machining [10–12]. Budak et al. [13] used a structural dynamics modification technique to efficiently update the FEM of flexible turbine blades. In addition to FEM, Kersting and Bierman [14] used mesh-free and modal models to simulate the dynamics of a turbine blade during peripheral milling. Meshreki et al. [15] modeled the thin-walled pocket structures by a 2D multi span plate (MSP) and presented a semi-analytical method to compute the natural frequencies of the structure. Compared to FEM-based methods, the MSP model offers ten to 20 times higher computational efficiency, but less versatility to model pockets with complex geometries.

✉ Keivan Ahmadi
kvahmadi@uvic.ca

¹ Department of Mechanical Engineering, University of Victoria, Victoria, British Columbia V8W 2Y2, Canada

In this paper, finite strip modeling (FSM) [16] is used to model thin-walled structures in pocket milling operations. FSM is a semi-analytical method in which the structure is discretized only in the transverse direction. The presented method combines the high computational efficiency of the MSP model and the versatility of FEM-based methods. The accuracy and efficiency of FSM in modeling the varying dynamics of pocket structures is verified by comparing its performance against FEM and MSP in multiple case studies. Additionally, the accuracy of the presented modeling approach is verified using the experimental results presented by Meshreki et al. in [15].

The application of FSM to model pocket structures is explained in the next section. Also, in Section 2, the constructed FSM is used to compute the frequency response functions (FRF) and to determine the stability of vibrations along the toolpath. The comparison of the performances of FSM, FEM, and MSP models is provided in Section 3.

2 Finite strip modeling (FSM)

Common aerostructures such as ribs and spars consist of a series of pockets with the general shape shown in Fig. 1. In this paper, the methodology will be explained using a single pocket with four sides, but the presented approach is applicable to general structures with multiple pockets as well. In the finishing stages, the thickness to length (or width) ratio of each side of the pocket is assumed to be small enough so that each side can be modeled using Kirchhoff's thin plate theory [17]. Moreover, because chip thickness and cutting forces are mainly affected by the out-of-plane deflections ($w(x,y)$) of the workpiece, the transverse vibrations of the plate (membrane deflections) are neglected.

In finite strip modeling (FSM), the structure is discretized in the transverse (X) direction by narrow strips of equal length Δx as shown in Fig. 1. Three coordinate systems are used in the following derivation: the global coordinate system ($X_0Y_0Z_0$), attached to the pocket corner, is used to describe the general geometry of the pocket; the local plate coordinate system (XY), attached to each side of the pocket, is used to describe the locations and dimensions of finite strips; and the local strip coordinate system (UV), attached to each strip on the plate, is used to describe the distribution of the deflection field, $w(x,y)$, inside each strip. Because the wall thickness can be different at various parts of the strip, each strip is assumed to consist of N_i spans with various thicknesses, t_i ($i=1..N_i$). For example, the strip shown in Fig. 1 consists of two spans with $t_1=t$ and $t_2=t'$. Considering that usually the base plate of the workpiece is firmly attached to the machine's table, clamped-free boundary conditions are assumed for each side of the pocket. Consequently,

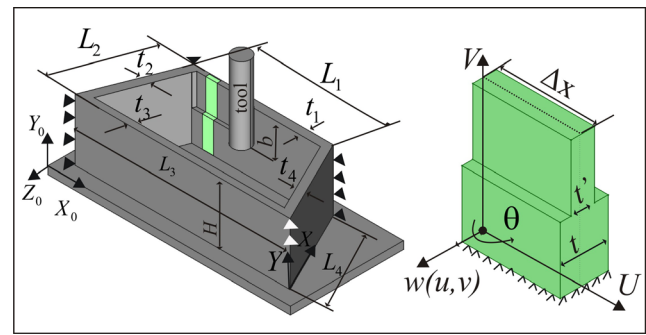


Fig. 1 a General geometry of pocket structures. b Finite Strip

within each strip, the displacement field in the longitudinal direction is approximated by a series of trigonometric functions ($Y_p(v)$) that satisfy clamped-free boundary conditions:

$$w(u, v, t) = \sum_{p=1}^m f_p(u, t) Y_p(v); \quad (1)$$

$$Y_p(v) = 1 - \cos(p-0.5)\pi(v/H)$$

, where $w(u,v,t)$ is the 2D distribution of the lateral vibrations of the neutral plane. The approximation of Eq. (1) converts the problem of finding the 2D displacement field, $w(u,v,t)$, into the much simpler problem of finding the 1D displacement field, $f_p(u,t)$, associated with each term of the trigonometric expansion. Similar to the Euler-Bernouli beam element, $f_p(u,t)$ is approximated by polynomial shape functions and two degrees of freedom (DOF) at each nodal line: w_{1p} and θ_{1p} at $u=0$, and w_{2p} and θ_{2p} at $u=\Delta x$:

$$w(u, v, t) = \sum_{p=1}^m \mathbf{S}_p(u, v) \mathbf{d}_p(t); \quad \mathbf{S}_p(u, v)$$

$$= [S_1(u) \quad S_2(u) \quad S_3(u) \quad S_4(u)] Y_p(v); \quad \mathbf{d}_p(t)$$

$$= \{w_{1p}(t) \quad \theta_{1p}(t) \quad w_{2p}(t) \quad \theta_{2p}(t)\}^T; \quad \bar{u} = u/\Delta x \quad (2)$$

$$S_1 = \left(1 - 3\bar{u}^2 + 2\bar{u}^3\right) \quad S_2 = \bar{u} \left(1 - 2\bar{u} + \bar{u}^2\right)$$

$$S_3 = \left(3\bar{u}^2 - 2\bar{u}^3\right) \quad S_4 = \bar{u} \left(\bar{u}^2 - \bar{u}\right)$$

Note that each node of plate elements in FEM has 3DOF consisting of the lateral deflection and two rotations around the U and V axis; but each nodal line in FSM has only 2DOF, because the rotation around U is accounted for by the continuous function in the longitudinal direction, $Y_p(v)$. As will be shown in the case studies of Section 3, this reduction in the number of DOF results in a tremendous saving in the required computation load.

2.1 Mass and stiffness matrices

Similar to FEM, the stiffness and mass matrices of the strip are obtained by the minimization of the bending strain and kinetic energy functions, respectively [17, 18]. The bending strain energy of the strip is expressed as follows:

$$U = \frac{1}{2} \int_V \{\varepsilon\}^T \{\sigma\} dV; \quad \{\sigma\} = \mathbf{D}\{\varepsilon\};$$

$$\mathbf{D} = \frac{E}{(1-\nu^2)} \begin{bmatrix} 1 & \nu & 0 \\ \nu & 1 & 0 \\ 0 & 0 & (1-\nu)/2 \end{bmatrix}; \quad (3)$$

, where $\{\sigma\}$ and $\{\varepsilon\}$ are bending stress and strain vectors, and E and ν are Young's modulus and Poisson's ratio, respectively. In this paper, for Aluminum 6060, they are $E=69$ GPa and $\nu=0.3$. Although usually the thickness is reduced from one side of the plate, we assume that the overall thickness of the plate is reduced simultaneously from both sides and thus the location of the neutral axis remains unchanged. The effect of this simplifying assumption on the computed natural modes was shown to be negligible in [15]. Based on this assumption and according to Kirchhoff's thin plate theory, bending strains, $\{\varepsilon\}$, are expressed in terms of the partial derivatives of the lateral displacement field as below:

$$\{\varepsilon\}^T = \{\varepsilon_u \quad \varepsilon_v \quad \gamma_{uv}\}^T;$$

$$\varepsilon_u = -z \frac{\partial^2 w}{\partial u^2}; \quad \varepsilon_v = -z \frac{\partial^2 w}{\partial v^2}; \quad \gamma_{uv} = 2z \frac{\partial^2 w}{\partial u \partial v} \quad (4)$$

By substituting the discrete approximation of the displacement field from Eq. (2) in Eq.(4), the bending strain vector is obtained in terms of the derivatives of the shape functions, \mathbf{B}_p , and the vector of nodal displacements, \mathbf{d}_p :

$$\{\varepsilon\} = z \sum_{p=1}^m \mathbf{B}_p \mathbf{d}_p;$$

$$[\mathbf{B}_p]_{3 \times 4} = \left[-\frac{\partial^2 \mathbf{S}_p}{\partial u^2} \quad -\frac{\partial^2 \mathbf{S}_p}{\partial v^2} \quad 2 \frac{\partial^2 \mathbf{S}_p}{\partial u \partial v} \right]^T \quad (5)$$

Substituting the bending strain terms from Eq. (5) in Eq. (3) and rearranging the integral into a matrix form leads to the following expression of the strain energy:

$$U = \sum_{p=1}^m \sum_{q=1}^m \frac{1}{2} (\mathbf{d}_p)^T \mathbf{k}_e^{pq} \mathbf{d}_q; \quad \mathbf{k}_e^{pq} = \sum_{i=1}^{N_i} \mathbf{k}_i^{pq}$$

$$\mathbf{k}_i^{pq} = \frac{t_i^3}{3} \left(\int_{u=0}^{\Delta x} \int_{v=v_i}^{v_{i+1}} \mathbf{B}_p^T \mathbf{D} \mathbf{B}_q du dv \right), \quad v_1 = 0, v_{N_i+1} = H \quad (6)$$

, where \mathbf{k}_e^{pq} is a 4×4 matrix representing the stiffness matrix elements associated with the four DOFs corresponding to Y_p and Y_q .

The kinetic energy of the strip in terms of the lateral displacement field is

$$T = \frac{1}{2} \rho \int_V \dot{w}^2 dV; \quad \dot{w} = \frac{\partial w(u, v, t)}{\partial t} = \sum_{p=1}^m \mathbf{S}_p \dot{\mathbf{d}}_p \quad (7)$$

, where ρ stands for the density of the workpiece material. In this paper, for Aluminum 6060, $\rho=2700$ Kg/m³. The mass matrix of the strip is obtained by substituting the discrete approximation of the displacement field from Eq. (2) in Eq. (7) and rearranging the integral into the following matrix form:

$$T = \sum_{p=1}^m \sum_{q=1}^m \frac{1}{2} \mathbf{d}_p^T \mathbf{m}_e^{pq} \mathbf{d}_q; \quad \mathbf{m}_e^{pq} = \sum_{i=1}^{N_i} \mathbf{m}_i^{pq}$$

$$\mathbf{m}_i^{pq} = \rho t_i \left(\int_{u=0}^{\Delta x} \int_{v=v_i}^{v_{i+1}} \mathbf{S}_p^T \mathbf{S}_q du dv \right), \quad v_1 = 0, v_{N_i+1} = H \quad (8)$$

, where \mathbf{m}_e^{pq} is a 4×4 matrix containing the mass matrix elements that correspond with the four DOF associated with Y_p and Y_q . The elements of \mathbf{m}_e^{pq} and \mathbf{k}_e^{pq} for $p, q=1..m$ are substituted in their corresponding locations in the $4m \times 4m$ mass and stiffness matrices of the strip. The global $4.m.N_s \times 4.m.N_s$ mass and stiffness matrices of the pocket (\mathbf{M} and \mathbf{K} , respectively) are created by assembling the strip matrices similar to FEM. N_s is the total number of the strips on the pocket. Details of the computations and assembly are available in [16].

2.2 Boundary conditions

Boundary conditions in the longitudinal direction are assumed to be clamped at $y=0$ and free at $y=H$:

$$w(x, 0, t) = 0; \quad \left. \frac{\partial w}{\partial y} \right|_{y=0} = 0;$$

$$\left. \frac{\partial^2 w}{\partial y^2} \right|_{y=H} = 0; \quad \left. \frac{\partial^3 w}{\partial y^3} \right|_{y=H} = 0 \quad (9)$$

These conditions are satisfied by the chosen trigonometric basis functions, $Y_p(v)$. Because the membrane deflections are neglected in this analysis, each corner of the pocket is assumed to be simply supported to satisfy continuity conditions:

$$w(0, y, t) = 0; \quad w(L_i, y, t) = 0; \quad i = 1..4 \quad (10)$$

Simply supported boundary conditions at the corners are fulfilled by eliminating the rows and columns of the global mass and stiffness matrices corresponding with the lateral displacement at the corners—similar to applying homogeneous boundary conditions in FEM.

Once the boundary conditions are applied, natural frequencies are obtained from the eigenvalues of the global mass and stiffness matrices:

$$(\mathbf{K} - \mathbf{M}\omega_r^2)\{\mathbf{V}_r\} = 0; \quad r = 1, 2, \dots, 2m(N_s + 1) \quad (11)$$

, where ω_r is the angular speed of mode r and $\{\mathbf{V}_r\}$ is its corresponding eigenvector.

2.3 Frequency response functions (FRF)

The direct and cross FRFs (α_{ij}) between any two arbitrary points, i and j , are defined in terms of the structure's modal properties [18]:

$$\alpha_{ij}(\omega) = \frac{w(u_i, v_i)}{F_j} = \sum_{r=1}^{N_r} \frac{\phi_r(u_i, v_i)\phi_r(u_j, v_j)}{\omega_r^2 - \omega^2 + 2i\xi_r\omega\omega_r} \quad (12)$$

, where ϕ_r is the mass-normalized mode shape, ξ_r is the modal damping ratio, u_i and v_i are the u and v coordinates of point i in its corresponding strip coordinate system (similarly for point j), and N_r is the number of natural modes considered in synthesizing the FRF. In Eq. (12), ϕ_r is constructed using the mass-normalized eigenvectors of the global mass and stiffness matrices, $\{\mathbf{V}_r\}$, as follows:

$$\phi_r(u_i, v_i) = \sum_{p=1}^m \mathbf{S}_p(u_i, v_i)\bar{\mathbf{d}}_p; \quad \bar{\mathbf{d}}_p = \begin{bmatrix} \bar{w}_{1p} & \bar{\theta}_{1p} & \bar{w}_{2p} & \bar{\theta}_{2p} \end{bmatrix}^T \quad (13)$$

, where \bar{w}_{1p} , $\bar{\theta}_{1p}$, \bar{w}_{2p} and $\bar{\theta}_{2p}$ are the elements of the eigenvector $\{\mathbf{V}_r\}$ that correspond with the two nodes of the strip on which point i is located.

2.4 Stability

Figure 2 shows a schematic of the tool and workpiece engagement at an arbitrary cutter location of the toolpath. This figure shows the tool in a semi-finishing pass, in which the initial wall thickness (t_0) is reduced to a semi-finished thickness of t_{sf} . Wall thickness reduces further to t_f in the finishing pass. H_t is the distance of the tool tip from the top edge of the pocket. The tool's diameter is designated by D , and the total number of flutes by N_f . The tool is assumed to be fully rigid, but the workpiece is flexible in the direction normal to the wall. The axial engagement of the tool, b , is divided into N_a disks of equal thickness $\Delta b = \frac{b}{N_a}$. A linear mechanistic force model is used to describe the tangential (F_t) and radial (F_r) cutting forces that are applied on each tooth ($j=1..N_f$) of each axial element ($i=1..N_a$) [19]:

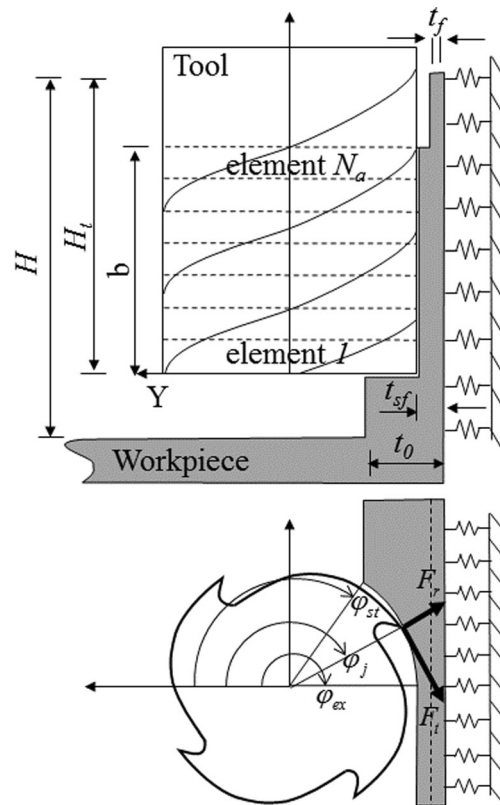


Fig. 2 Vibration model of thin-walled machining

$$\begin{aligned} F_t &= K_{tc}\Delta b h_j + K_{te}\Delta b \\ F_r &= K_{rc}\Delta b h_j + K_{re}\Delta b \end{aligned} \quad (14)$$

, where K_{tc} and K_{rc} are the cutting force coefficients, and K_{te} and K_{re} are the edge force coefficients [19]; h_j is the chip thickness:

$$\begin{aligned} h_j &= s_t \sin \varphi_j(t) - \Delta w_i \cos \varphi_j(t); \quad \Delta w_i \\ &= w_i(u_i, v_i, t) - w_i(u_i, v_i, t-T) \end{aligned} \quad (15)$$

As shown in Fig. 2, $\varphi_j(t)$ is the angular immersion of the j^{th} tooth at each moment. The radial and tangential elemental forces are assumed to be concentrated at the middle of each axial element. The first term in Eq. (15) shows the portion of the chip thickness that is generated by the feed motion of the tool, s_t [feed/tooth]. This term is also known as the static chip thickness. The second term shows the regenerative part, which is produced by the vibration of the workpiece ($w_i(t)$) and the undulations left on the surface by the vibrations at the previous tooth passing ($w_i(t-T)$). T is the tooth passing period. The static term of the chip thickness and the edge forces do not affect the stability of vibrations, and thus, they will be ignored in stability analysis. The tangential and radial forces generated by each of the flutes are projected in

the direction normal to the plate and summed altogether to obtain the overall normal cutting force that is exerted on each axial element:

$$F_i = A_i(t) \cdot \Delta w_i; \quad i = 1..N_a$$

$$A_i(t) = \sum_{j=1}^{N_f} \frac{\Delta b}{2} g_j \left(K_{tc} \sin 2\varphi_j - K_{rc} (1 + \cos 2\varphi_j) \right) \quad (16)$$

g_j is a unit step function that determines whether each

flute is engaged with the workpiece:

$$g_j = \begin{cases} 0 & \text{otherwise} \\ 1 & \varphi_{st} < \varphi_j < \varphi_{ex} \end{cases} \quad (17)$$

φ_{st} and φ_{ex} are the start and exit angles, shown in Fig. 2. In Eq. (16), $A_i(t)$ is a periodic function at the tooth passing period, T . Following the zero order frequency domain solution of [20], $A_i(t)$ is approximated by the average term in its Fourier expansion.

$$A_0 = \frac{N_f \Delta b}{8\pi} [(-K_{tc} \cos 2\varphi_{ex} - 2K_{rc} \varphi_{ex} - K_{rc} \sin 2\varphi_{ex}) - (-K_{tc} \cos 2\varphi_{st} - 2K_{rc} \varphi_{st} - K_{rc} \sin 2\varphi_{st})] \quad (18)$$

Substituting the approximation of Eq. (18) in Eq. (16), the elemental cutting forces are expressed in terms of the wall deflections using the following equation:

$$\mathbf{F} = \mathbf{A}_0 \Delta \mathbf{w}; \quad \mathbf{F} = \begin{bmatrix} F_1 \\ \vdots \\ F_{N_a} \end{bmatrix}, \Delta \mathbf{w} = \begin{bmatrix} \Delta w_1 \\ \vdots \\ \Delta w_{N_a} \end{bmatrix} \quad (19)$$

In the frequency domain, Eq. (19) is converted into:

$$\mathbf{F}(\omega_c) = \mathbf{A}_0 (1 - e^{-i\omega_c T}) \mathbf{w}(\omega_c) \quad (20)$$

According to Eq. (12), the deflection vector in the frequency domain, $\mathbf{w}(\omega_c)$, is related to the force vector, $\mathbf{F}(\omega_c)$, through the FRF matrix:

$$\mathbf{F}(\omega_c) = \mathbf{A}_0 (1 - e^{-i\omega_c T}) \mathbf{\Phi} \left(\Omega^2 - \omega_c^2 \mathbf{I}_{N_r \times N_r} + \mathbf{Z} i \omega_c \right) \mathbf{\Phi}^T \mathbf{F}(\omega_c)$$

$$\Omega = \begin{bmatrix} \omega_1 & \cdots & 0 \\ & \ddots & \\ 0 & & \omega_r \end{bmatrix}; \mathbf{Z}$$

$$= \begin{bmatrix} 2\xi_1 \omega_1 & \cdots & 0 \\ & \ddots & \\ 0 & & 2\xi_r \omega_r \end{bmatrix}; \mathbf{I}_{N_r \times N_r} = \begin{bmatrix} 1 & \cdots & 0 \\ & \ddots & \\ 0 & & 1 \end{bmatrix} \quad (21)$$

, where $\mathbf{\Phi}$ is the mode shape matrix:

$$\mathbf{\Phi}_{N_a \times N_r} = \begin{bmatrix} \phi_1(u_1, v_1) & \phi_2(u_1, v_1) & \cdots & \phi_{N_r}(u_1, v_1) \\ \phi_1(u_2, v_2) & \phi_2(u_2, v_2) & \cdots & \phi_{N_r}(u_2, v_2) \\ \vdots & \vdots & \cdots & \vdots \\ \phi_1(u_{N_a}, v_{N_a}) & \phi_2(u_{N_a}, v_{N_a}) & \cdots & \phi_{N_r}(u_{N_a}, v_{N_a}) \end{bmatrix} \quad (22)$$

The nontrivial solution of Eq. (21) leads to the characteristic equation of the regenerative vibrations in the direction normal to the plate:

$$|\mathbf{I}_{N_a \times N_a} - \mathbf{A}_0 (1 - e^{-i\omega_c T}) \mathbf{\Phi} (\Omega^2 - \omega_c^2 \mathbf{I}_{N_r \times N_r} + \mathbf{Z} i \omega_c) \mathbf{\Phi}^T| = 0; \quad (23)$$

At each axial depth of cut, b , and tooth passing period, T , the roots of the characteristic equation are determined by sweeping the chatter frequency, ω_c , in a frequency range that covers all of the dominant vibration modes. Subsequently, the stability of vibrations is determined from the roots of the characteristic equation according to the Nyquist stability criterion [21].

3 Results

3.1 FEM and FSM modeling of a cantilever plate

In this section, the natural frequencies of a cantilever Kirchhoff plate are computed analytically, using FEM, and using the presented FSM. The dimensions of the plate are shown in Fig. 3. The plate thickness is assumed to be 10 mm. In FEM, five elements are used in the transverse (X) direction and the convergence of the first ten natural frequencies are studied by increasing the number of elements in the longitudinal (Y) direction from two to 20 elements. The analytical solution of the free vibrations of cantilever plates was presented in [22]. This analytical solution is used here to compute the natural frequencies of the plate shown in Table 1. The error percentage shown in Fig. 3 is the deviation of the tenth natural frequency that is computed using FSM or FEM from their corresponding analytical values. The error percentage converges to a constant value by increasing the number of elements in FEM. To achieve a less than 0.1 % variation in the computed natural frequencies, FEM requires at least 14 elements in the longitudinal direction. The natural frequencies of the first ten modes and their deviation from analytical values are shown in Table 1. Consistently, five strips are used in FSM and the number of trigonometric terms (m) is increased from two to 20 terms to study the convergence of the computed natural frequencies. As shown in Fig. 3, the error percentage converges to a constant value when m increases. To achieve a less than 0.1 % variation in the computed natural frequencies for all of the first ten modes, $m=9$ harmonic terms are required in FSM. Computed natural frequencies for the first

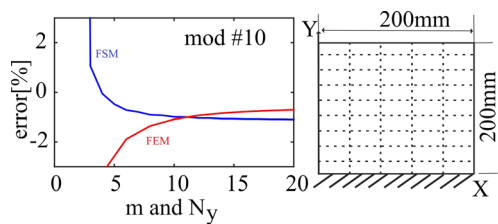


Fig. 3 Convergence diagrams of FEM and FSM for a cantilever plate case study; plate thickness 10 mm, $E = 69$ GPa, $\nu = 0.3$, and $\rho = 2700$ Kg/m³

ten modes and their deviation from analytical values (error) are shown in Table 1. Both of the methods result in similarly accurate natural frequencies when 14 longitudinal elements are used in FEM and nine harmonic terms are used in FSM; however, FEM involves $15 \times 3 \times 6 = 270$ DOF and FSM involves $6 \times 2 \times 9 = 108$ DOF. This 60 % reduction in the number of DOF results in approximately 10 times faster computation of the eigenvalues. In addition, FSM requires less computational time for re-meshing, which contributes further to increasing the computational efficiency of the presented method.

3.2 FEM and MSP models of a pocket

In this section, FSM is used to obtain the natural mode shapes of an Aluminum 6060 pocket with $L_1 = 200$, $L_2 = 130.6$, $L_3 = 58$, $L_4 = 115.6$, $t_1 = 3$, $t_2 = 3.5$, $t_3 = 4$, $t_4 = 2$, and $H = 80$ mm and $\alpha = 40^\circ$. Natural frequencies of this pocket after machining $b = H_t = 26.7$ mm from the top of its first side were computed using an MSP model in [15]. The thickness of the machined depth is reduced from 3 to 2 mm. The values of the first ten natural frequencies that were computed using the MSP model are shown in Table 2. Also shown in this table are the natural frequencies that were computed using a commercial FEM software. The deviation of the natural frequencies computed using MSP and FSM from their corresponding FEM values are listed as error percentage in Table 2. In the FSM solution, the accuracy of the computed natural frequencies depends on the number of strips and the number of trigonometric terms, m , that are used in computations. The average and maximum errors of the first ten natural frequencies computed using MSP are 2.5 and 4 %, respectively, as reported in [15]. Figure 4 shows the average and maximum error across all of the first ten natural frequencies of the pocket

computed using FSM while the number of strips and trigonometric terms increase. As shown in this figure, increasing the overall number of strips from 22 to 26 does not make a significant difference in the converged error percentage; therefore, 22 strips are used in FSM. With 22 strips, when $m = 4$ the average and maximum errors are 2.4 and 3.9 %, which are below the average and maximum errors of MSP results (i.e., 2.5 % and 4 %); therefore, $m = 4$ trigonometric terms are used in FSM. Table 2 shows the first ten natural frequencies resulting from the FSM and their deviation from the FEM results. Also, the first three mode shapes of the pocket are shown in this figure.

3.3 Forced and regenerative vibrations

The accuracy of FSM in predicting the dynamic deflections of thin-walled structures is verified using the experimental results presented in [23]. In their experiments, Meshrahi et al. used an Aluminum 6060 square pocket of $H = 50$ mm height, $L_1 = 121$, $L_2 = 81$, $L_3 = 121$, $L_4 = 81$, $t_1 = 4$, $t_2 = 2$, $t_3 = 4$, and $t_4 = 3$ mm. The pocket was machined using a $D = 15.875$ mm, two-flute end mill with 30° helix angle. Down milling was used in the experiments, and thus, $\varphi_{st} = \pi - \cos^{-1}(\frac{D-b_r}{D})$ and $\varphi_{ex} = \pi$, where b_r is the radial depth of cut. According to Fig. 2 the radial depth of cut in semi-finishing passes is $t_0 - t_{sf}$ and in finishing passes equals to $t_{sf} - t_f$. The vibrations of the first side of the pocket during semi-finishing passes were measured using three contactless position probes installed at $(x = 62, y = 43)$, $(x = 30, y = 43)$, and $(x = 92.5, y = 41.5)$ millimeters. Probes 1 and 2 were KAMAN-UEP, and probe 3 was BENTLY-3300 REBAM. The thickness of the first side was reduced from 4 to 3.2 mm in 25 semi-finishing and finishing passes. Then the thickness was reduced from 3.2 to 2.4 mm in another 25 semi-finishing and finishing passes. The axial depth of cut values in all of the finishing and semi-finishing passes were 2 mm. Radial depth of cut in semi-finishing passes were 0.6 and 0.2 mm in finishing passes. Each semi-finishing pass was followed by a finishing pass. Spindle speed was 9000 rev/min and feedrate was 0.2 mm/tooth. Figure 5 shows the measured dynamic deflections in three of the semi-finishing passes. The deflections shown in Fig. 5a, b were recorded during the semi-finishing pass that reduced the thickness from $t_0 = 3.2$ to $t_{sf} = 2.6$ mm. In Fig. 5a the tool tip was at $H_t = 10$ mm, and in

Table 1 The first ten natural frequencies [Hz] of the cantilever plate obtained analytically, using FEM and FSM

Mod#	1	2	3	4	5	6	7	8	9	10
Analytical	3.459	8.356	21.09	27.06	30.55	53.53	61.12	63.62	70.64	92.21
FEM (error %)	3.458	8.476	21.26	27.11	30.82	53.61	61.49	63.90	70.81	91.42
	(-0.02)	(1.45)	(0.82)	(0.19)	(0.88)	(0.15)	(0.60)	(0.44)	(0.25)	(-0.86)
FSM (error%)	3.460	8.141	21.06	26.91	30.05	52.57	61.09	63.63	70.24	91.35
	(0.039)	(-2.57)	(-0.13)	(-0.55)	(-1.64)	(-1.80)	(-0.55)	(0.021)	(-0.57)	(-0.93)

Table 2 The first ten natural frequencies [Hz] of the pocket structure obtained using FEM, FSM, and MSP [23]

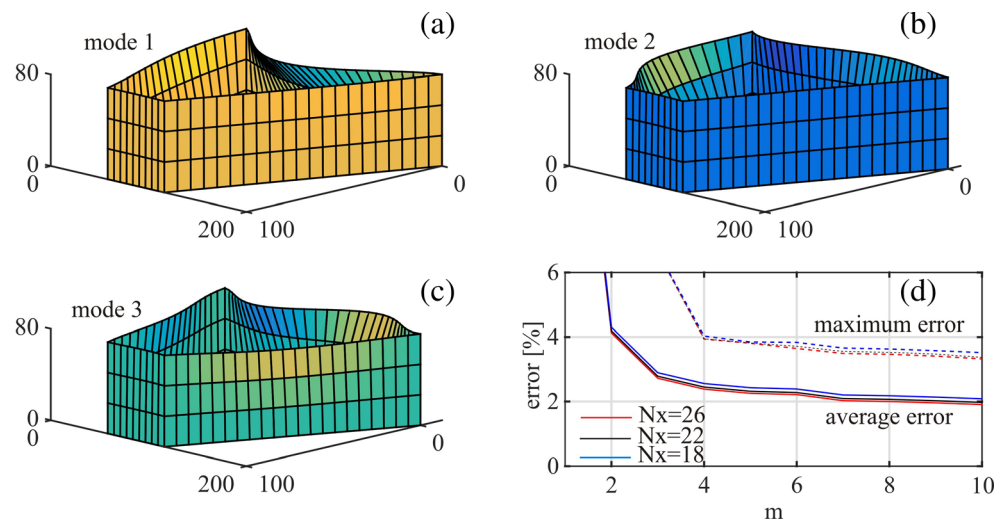
Mode	1	2	3	4	5	6	7	8	9	10
FEM	611	825	1004	1146	1762	2133	2215	2471	2516	2859
MSP	612	859	1026	1182	1783	2225	2265	2528	2581	2967
Error (%)	0.1	4	2.2	3.1	1.2	4.3	2.3	2.3	2.6	3.8
FSM	617	840	1028	1170	1789	2191	2250	2568	2615	2958
Error (%)	1.0	1.8	2.4	2.1	1.5	2.7	1.6	3.9	4	3.5

Fig. 5b, it was at $H_t=16$ mm. In Fig. 5c, the thickness was reduced from $t_0=4$ mm to $t_{sf}=3.4$ mm, and the tool tip was at $H_t=20$ mm. The experimentally measured deflection values shown in Fig. 5 are the maximum deflections that were recorded using each of the probes at different time frames while the tool travels across side one. Also shown in this figure are the maximum deflections predicted using the FSM at eight evenly spaced points along the tool path. Because the measured cutting force data are not available in [23], the cutting forces at each of the points shown in Fig. 5 were simulated using Cutpro—a specialized milling process simulation software. The linear cutting force model of Eq. (14) with $K_{tc}=731$ MPa, $K_{rc}=431$ MPa, $K_{re}=20$ N/mm and $K_{te}=35$ N/mm was used in simulations. These cutting force coefficients were identified through extensive cutting experiments in [24]. A sample of the simulated cutting forces is shown in Fig. 5d. The cross FRFs between the locations of the probes and the tool tip locations as the tool moves across side one are obtained from Eq. (12). The damping ratio of $\xi_r=0.07$ is used for all of the ten modes that are considered in computing the FRFs. A sample of the computed FRFs is also shown in Fig. 5d. Computed FRFs along with simulated forces were used in Cutpro to simulate workpiece vibrations. A sample of the simulated workpiece vibrations is demonstrated in Fig. 5d as well. Similar simulations were conducted for all of the points in Fig. 5a–c, and the maximum deflections at each point are shown this figure. The predicted maximum dynamic deflections agree with the values measured in the experiment of

Meshreki et al.[23]. Note that in all of the experiments of [23], the cutting conditions resulted in stable vibrations.

A case study is presented here to study the accuracy of the stability analysis approach presented in Section 2.4 in determining the stability of vibrations. In this case study, the thickness of the first side of the pocket is reduced from 4 to 2 mm. Ten passes with 5 mm depth of cut, $b_r=1.8$ mm radial depth of cut in semi-finishing, and 0.2 mm in finishing were used. The stability of vibrations at each cutter location along the toolpath were determined at a grid of spindle speeds between 5000 and 20000 rev/min. The stability diagrams in Fig. 6a show the border between stable and unstable cutter locations at each spindle speed. The red diagram shows the stability borders of the first semi-finishing pass ($H_t=5$ mm) and the blue diagram shows the stability borders in the second semi-finishing pass ($H_t=10$ mm). All of the cutter locations were stable in the third to tenth passes. The points inside the borders are unstable and the points outside of the borders are stable. Using a commercial personal computer with a 2.4-GHz processor, the stability diagrams of Fig. 6a were computed in less than 1 min, although the computation time depends on the computer's processor and the structure of the computer program.

Workpiece vibrations at two cutter locations were simulated using the Cutpro application in the second semi-finishing pass. The simulated vibrations are shown in Fig. 6c–f. As seen in the frequency spectrum of the simulated vibrations, when the tool is approximately at the middle of side one (tool position = 52 mm),

Fig. 4 a–c The first three mode shapes of the pocket structure obtained using FSM. d The convergence diagram of FSM in computing the first ten natural frequencies of the pocket

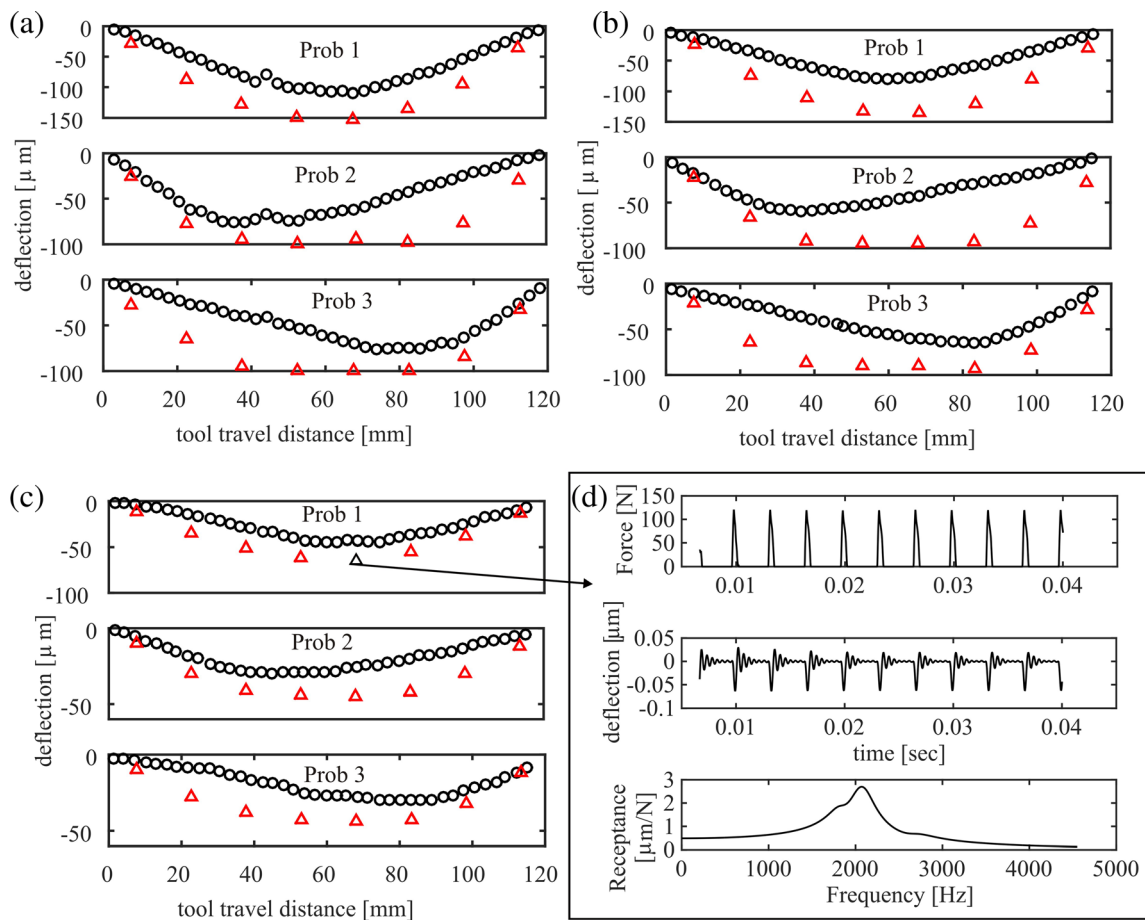


Fig. 5 Dynamic deflections at three points (probes 1–3) on the first side of the square pocket as the tool travels across side one. The experimental results are as reproduced from [23]. **a** $t_0 = 3.2$ mm, $t_{sf} = 2.6$ mm, $b = 2$ mm,

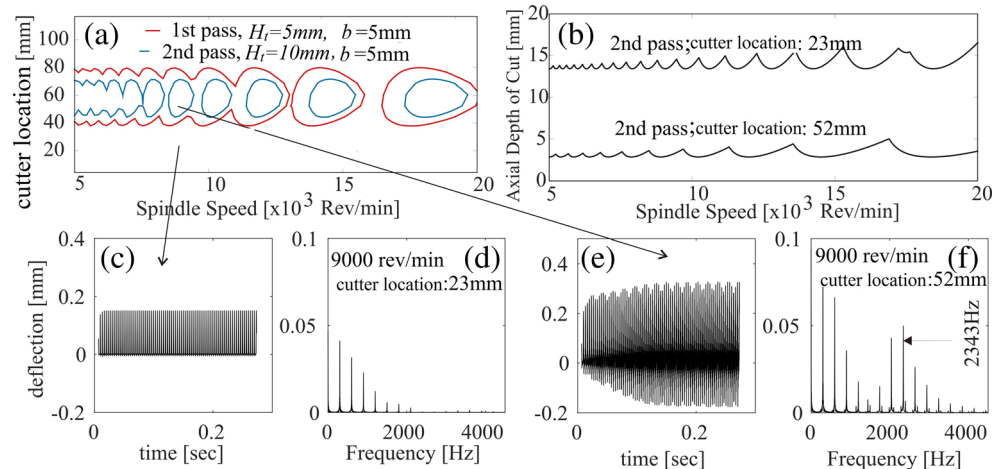
$H_t = 10$ mm. **b** $t_0 = 3.2$ mm, $t_{sf} = 2.6$ mm, $b = 2$ mm, $H_t = 16$ mm. **c** $t_0 = 4$ mm, $t_{sf} = 3.4$ mm, $b = 2$ mm, $H_t = 20$ mm; Feedrate 0.2 mm/flute and spindle speed 9000rev/min; material Aluminum 6060

vibrations become unstable at 2343 Hz. Stability lobes [19] at two cutter locations (23 and 52 mm) during the second semi-finishing pass are computed using Cutpro and are shown in Fig. 6b. At 52 mm the critical limit of stable axial depth of cut is below 5 mm, but at 23 mm, the critical limit is much higher than the 5-mm depth of cut assumed in this case study.

4 Conclusions

Finite strip models (FSM) of pocket structures were presented in this paper. FSM offers a significantly higher computational efficiency compared to FEM while preserving FEM's versatility in modeling complex geometries. The accuracy and efficiency of

Fig. 6 **a** Stability diagrams of the first two semi-finishing passes on the first side of the pocket **b** Stability lobes at two cutter locations. **c–f** Simulated vibrations at stable and unstable cutter locations



the presented FSM was validated by comparison against FEM and semi-analytical multi span plate (MSP) model [23]. Further investigation is required to study the performance of FSM in modeling the structural dynamics of large-scale aerostructures with complicated and curved geometries. The high computational efficiency and versatility of the presented method makes it suitable for integration in process optimization methods to increase the material removal rate without causing excessive dynamic deflections or unstable vibrations.

References

1. Yang Y, Wan M, Ma YC, Zhang WH (2016) An improved method for tool point dynamics analysis using a bi-distributed joint interface model. *Int J Mech Sci* 105:239–252
2. Schmitz TL, Donalson RR (2000) Predicting high-speed machining dynamics by substructure analysis. *CIRP Ann Manuf Technol* 49(1):303–308
3. Law M, Phani AS, Altintas Y (2013) Position-dependent multibody dynamic modeling of machine tools based on improved reduced order models. *J Manuf Sci Eng* 135(2):021008
4. Ertrk A, Ozguven HN, Budak E (2006) Analytical modeling of spindle-tool dynamics on machine tools using Timoshenko beam model and receptance coupling for the prediction of tool point FRF. *Int J Mach Tools Manuf* 46(15):1901–1912
5. Ahmadi K, Ahmadian H (2007) Modelling machine tool dynamics using a distributed parameter tool-holder joint interface. *Int J Mach Tools Manuf* 47(12–13):1916–1928
6. Ning H, Zhigang W, Chengyu J, Bing Z (2003) Finite element method analysis and control stratagem for machining deformation of thin-walled components. *J Mater Process Technol* 139(1–3):332–336
7. Rai JK, Xirouchakis P (2008) Finite element method based machining simulation environment for analyzing part errors induced during milling of thin-walled components. *Int J Mach Tools Manuf* 48(6):629–643
8. Ratchev S, Nikov S, Moualek I (2004) Material removal simulation of peripheral milling of thin wall low-rigidity structures using FEA. *Adv Eng Softw* 35(8–9):481–491
9. Tsai JS, Liao CL (1999) Finite-element modeling of static surface errors in the peripheral milling of thin-walled workpieces. *J Mater Process Technol* 94(2):235–246
10. Elbestawi MA, Sagherian R (1991) Dynamic modeling for the prediction of surface errors in the milling of thin-walled sections. *J Mater Process Technol* 25(2):215–228
11. Thevenot V, Arnaud L, Dessein G, Cazenave-Larroche G (2006) Integration of dynamic behaviour variations in the stability lobes method: 3D lobes construction and application to thin-walled structure milling. *Int J Adv Manuf Technol* 27(7–8):638–644
12. Arnaud L, Gonzalo O, Seguy S, Jauregi H, Peigné G (2011) Simulation of low rigidity part machining applied to thin-walled structures. *Int J Adv Manuf Technol* 54(5–8):479–488
13. Budak E, Tunç LT, Alan S, Özgüven HN (2012) Prediction of workpiece dynamics and its effects on chatter stability in milling. *CIRP Ann Manuf Technol* 61(1):339–342
14. Kersting P, Biermann D (2014) Modeling techniques for simulating workpiece deflections in NC milling. *CIRP J Manuf Sci Technol* 7(1):48–54
15. Meshreki M, Attia H, Kövecses J (2011) Development of a New model for the varying dynamics of flexible pocket-structures during machining. *J Manuf Sci Eng* 133(4):041002
16. Cheung YK (2013) Finite strip method in structural analysis. Elsevier, Amsterdam
17. Rao SS (2007) Vibration of continuous systems. John Wiley & Sons, Hoboken, New Jersey
18. Rao SS, Fook FY (1995) Mechanical vibrations (vol. 4). Addison-Wesley, New York
19. Altintas Y, Manufacturing Automation (2012) Metal cutting mechanics, machine tool vibrations, second. Cambridge University Press, New York
20. Budak E, Altintas Y (1998) Analytical prediction of chatter stability in milling—part I: general formulation. *J Dyn Syst Meas Control* 120(1):22
21. Eynian M, Altintas Y (2010) Analytical chatter stability of milling with rotating cutter dynamics at process damping speeds. *J Manuf Sci Eng* 132(2):021012
22. Gorman DJ (1976) Free vibration analysis of cantilever plates by the method of superposition. *J Sound Vib* 49(4):453–467
23. Meshreki M, Attia H, Kövecses J (2011) A New analytical formulation for the dynamics of multipocket thin-walled structures considering the fixture constraints. *J Manuf Sci Eng* 133(2):021014
24. Tsai MY, Chang SY, Hung JP, Wang CC (2015) Investigation of milling cutting forces and cutting coefficient for aluminum 6060-T6. *Comput Electr Eng* 000:1–11